Bulletin of Electrical Engineering and Informatics
Vol. 15, No. 2, April 2026, pp. 1114~1126
ISSN: 2302-9285, DOI: 10.11591/eei.v15i2.11306

Vertex and edge labelling strategies for graph-based computed tomography image denoising

Iwan Setiawan[1,2,5], Didi Rosiyadi[2,5], Rina Ratianingsih[3], Maulidyani Abu[3], Edy Tri Baskoro[4,5]
[1]Doctoral Program of Mathematics, Department of Mathematics, Faculty of Mathematics and Natural Sciences, Institut Teknologi Bandung, Bandung, Indonesia
[2]Research Center for Artificial Intelligence and Cyber Security, National Research and Innovation Agency, Bandung, Indonesia
[3]Department of Physics and Mathematics, Faculty of Mathematics and Natural Science, University of Tadulako, Palu, Indonesia
[4]Department of Mathematics, Faculty of Mathematics and Natural Sciences, Institut Teknologi Bandung, Bandung, Indonesia
[5]Center for Research Collaboration on Graph Theory and Combinatorics, Institut Teknologi Bandung-National Research and Innovation Agency-Universitas Indonesia, Bandung, Indonesia

Article Info

Article history:

Received Sep 1, 2025
Revised Feb 12, 2026
Accepted Mar 5, 2026

Keywords:

Computed tomography
Graph labelling
Graph signal processing
Image denoising
Spectral graph wavelet

ABSTRACT

Low-dose computed tomography (LDCT) reduces radiation exposure but introduces elevated noise and streak artifacts that degrade structural fidelity. This paper proposes a graph-based LDCT denoising framework that stabilizes graph construction through explicit vertex and edge labelling guided by paired full-dose CT (FDCT) data. The overlapping LDCT patches are modeled as vertices, and FD-guided affinities are used to build a structurally consistent adjacency matrix and a Laplacian spectrum that are less sensitive to noise. Denoising is performed by spectral filtering via spectral graph wavelet transform (SGWT), followed by overlap–add patch aggregation for image reconstruction. Experiments on paired LDCT/FDCT slices (318 pairs) show that FD-guided labelling improves denoising quality compared with conventional filters and non-guided graph baselines. Quantitative results demonstrate higher peak signal-to-noise ratio (PSNR)/structural similarity index measure (SSIM) with improved edge and feature preservation, indicating better structural boundary retention under noise suppression.

Corresponding Author:

Iwan Setiawan
Doctoral Program of Mathematics, Department of Mathematics
Faculty of Mathematics and Natural Sciences, Institut Teknologi Bandung
St. Ganesha 10, Bandung, Indonesia
Email: iwan022@brin.go.id

1. INTRODUCTION

Computed tomography (CT) is a primary modality for high-resolution cross-sectional imaging, but acquisition dose strongly influences image quality. Low-dose CT (LDCT) reduces radiation exposure; however, reduced photon counts amplify noise and streak artifacts, which degrade edge integrity and suppress fine anatomical structures [1]. Therefore, reliable LDCT denoising requires strong noise attenuation without sacrificing directional boundaries and weak textures [2], [3].

Conventional denoising methods can reduce noise, but they often over-smooth subtle structures that are important for interpretation [4]. Although deep learning methods can achieve impressive restoration performance, they typically require large curated datasets and substantial computational resources and may generate spurious structures under domain shift, raising concerns about robustness and interpretability in safety-critical imaging workflows [5], [6]. Recent reviews have further emphasized the gap between objective scores, such as peak signal-to-noise ratio (PSNR) and structural similarity index measure (SSIM),

and perceptual or diagnostic fidelity, highlighting the risk of overly smooth reconstructions when purely distortion-based losses are optimized [7]. Recent work has also explored zero-shot or prior-based approaches to reduce dependence on paired training data [8].

Graph-based image processing represents images on non-Euclidean domains, where pixels or patches are treated as vertices and their relationships are encoded as weighted edges. Within graph signal processing (GSP), denoising can be performed by spectral filtering using Laplacian operators derived from these weights [9]-[11]. However, most graph-based denoisers construct edge weights directly from noisy LDCT intensities, allowing noise to distort the adjacency structure and Laplacian spectrum and reducing spectral filtering and edge preservation reliability [12]. Graph learning and graph representation methods have advanced rapidly [13]. However, to the best of our knowledge, only a few studies have systematically investigated explicit vertex and edge labelling strategies for CT denoising that control graph construction while balancing noise suppression and structural fidelity.

This paper proposes FD-guided vertex and edge labelling strategies for patch-based graphs in LDCT denoising to address this gap. Structural information from paired full-dose CT (FDCT) data is transferred to guide adjacency construction, stabilizing the Laplacian spectrum and enabling reliable multiscale filtering via spectral graph wavelet transform (SGWT) [14]. The main contributions of this work are: i) an FD-guided labelling formulation that reduces noise-induced distortion of the Laplacian spectrum, ii) a SGWT-based denoising pipeline built on the stabilized graph, and iii) quantitative evaluation using PSNR, SSIM, and structure-preservation metrics across paired LDCT/FDCT slices. This approach provides an interpretable denoising mechanism tailored to CT imaging, improving structural fidelity while avoiding task-specific supervised training on large paired datasets, typical of many learning-based methods [15], [16].

2. METHOD

2.1. Overview and algorithm of the proposed full-dose-guided graph denoising pipeline

LDCT denoising is formulated as spectral filtering of a graph signal defined on a patch-based representation of each CT slice. Each LDCT slice is partitioned into overlapping patches; each patch becomes a graph vertex, and edges connect neighboring patches. The central idea is FD-guided graph construction, in which structural information from the paired FDCT slice is used to guide edge weights so that the graph topology reflects anatomical structure rather than LDCT noise, thereby stabilizing the Laplacian spectrum and improving the reliability of subsequent spectral filtering. Denoising is performed in the SGWT domain, and the final image is reconstructed by the overlap-add aggregation of denoised patches. Figure 1 summarizes the end-to-end workflow.

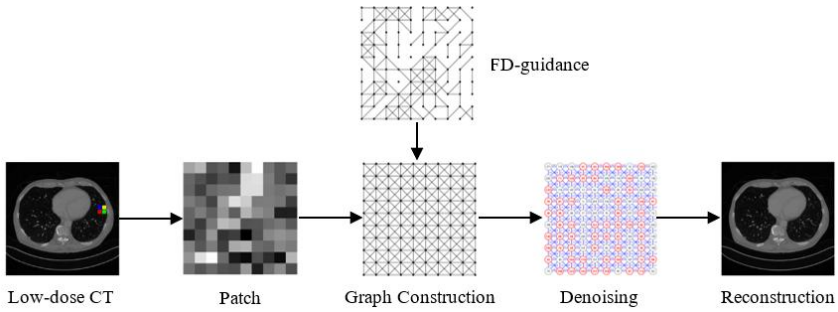

Figure 1. FD-guided denoising workflow

Algorithm 1 summarizes the end-to-end procedure, including patch extraction, FD-guided adjacency construction, normalized Laplacian computation, SGWT-domain shrinkage, and overlap–add reconstruction.

Algorithm 1. FD-guided patch-graph SGWT denoising

Input: LDCT slice I_L, paired FDCT slice I_F, patch size p, stride s, neighborhood rule (8-neighbor) $\mathcal{N}(i)$, similarity scales σ and τ, SGWT scales S, Chebyshev order M, shrinkage operator $T(\cdot)$, overlap weights (uniform).

Output: Denoised slice $\hat{I}_L$

Step 1. Extract overlapping patches from I_L: obtain $\{P_i^L\}$ and descriptors $\mathbf{x}_i = \mathrm{vec}(P_i^L)$.

Step 2. Extract aligned FDCT patches from I_F: obtain $\{P_i^F\}$ and descriptors $\mathbf{f}_i = \mathrm{vec}(P_i^F)$.

Step 3. Construct sparse adjacency W on 8-neighbor edges:
- Non-FD: $w_{ij} = \exp(-\| \mathbf{x}_i - \mathbf{x}_j \|_2^2/\sigma^2)$, for $j \in \mathcal{N}(i)$
- FD-guided: $w_{ij} = \exp(-\| \mathbf{x}_i - \mathbf{x}_j \|_2^2/\sigma^2) \cdot \exp(-\| \mathbf{f}_i - \mathbf{f}_j \|_2^2/\tau^2)$, for $j \in \mathcal{N}(i)$.

Step 4. Compute the normalized Laplacian $L = I - D^{-1/2}WD^{-1/2}$.
Step 5. Apply SGWT at scales S (Chebyshev order M), shrink coefficients with $T(\cdot)$, and invert SGWT to obtain denoised patch signals.
Step 6. Reconstruct $\hat{I}_L$ by uniform overlap–add aggregation of denoised patches.
Step 7. Return $\hat{I}_L$.

2.2. Dataset and experimental setting

For objective evaluation, the experiments used a public paired LDCT/FDCT dataset consisting of aligned 2D slices [17]. LDCT slices are the noisy inputs; the corresponding FDCT slices serve both structural guidance for graph construction and reference targets for evaluation metrics. We used 636 images from a single patient (318 LDCT–FDCT pairs). This controlled setting isolates the effect of FD-guided labelling under consistent anatomical and acquisition conditions. We acknowledge that this design limits generalization across patients, scanners, and dose protocols. Future work will validate robustness on multi-patient cohorts using cross-patient splits and stratification by anatomy and dose level. Public LDCT datasets with paired routine-dose references or simulated low-dose measurements are widely used for method development and objective benchmarking [18], [19].

2.3. Patch-based vertex construction and labelling

Let $I_L \in \mathbb{R}^{M\times N}$ denote an LDCT slice and $I_F \in \mathbb{R}^{M\times N}$ its paired FDCT slice. We extract overlapping square patches of size $p \times p$ from I_L with stride s. Let $P_i^L \in \mathbb{R}^{p\times p}$ denote the i-th LD patch and $\mathrm{vec}(\cdot)$ be column-wise vectorization. The LD patch descriptor is defined as follows: $\mathbf{x_i} = \mathrm{vec}(P_i^L) \in \mathbb{R}^{p^2}$.

Each patch corresponds to a vertex v_i in the graph $G = (V, E, W)$, where $V = \{v_1, \ldots, v_n\}$. The vertex labels are the patch descriptors x_i, so the graph signal to be denoised is $x = [x_1, \ldots, x_n]$. Figure 2 illustrates the processes of patch extraction, vectorization, and vertex formation. Specifically, Figures 2(a) and (b) show how a CT slice is partitioned into overlapping patches, which serve as the fundamental units of graph construction. In Figure 2(c), each patch is vectorized into a descriptor that captures both intensity and contextual features. The descriptors are subsequently mapped to graph vertices in Figure 2(d), where the vertex labels encode localized structural information such as tissue density or texture. This representation ensures that anatomical details are preserved within the graph while providing a robust foundation for spectral denoising.

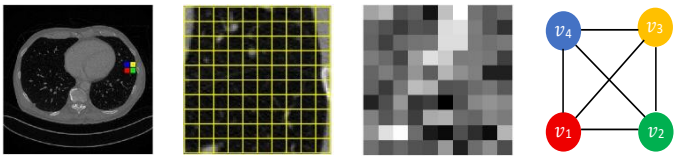

(a) (b) (c) (d)

Figure 2. Vertex labelling in patch-based graph construction; (a) CT slice with selected regions of interest, (b) overlapping patch extraction with stride, (c) example patch vectorization, and (d) graph vertices formed from patch descriptors

2.4. Full-dose-guided edge labelling and construction of sparse adjacency

2.4.1. Edge set (sparse topology)

We use a fixed 8-neighbor lattice on the patch grid to keep the topology reproducible and computationally efficient: each vertex v_i connects only to its spatial 8-neighbors $\mathcal{N}(i)$. $E = \{(i,j): j \in \mathcal{N}(i)\}, w_{ij} = 0$ if $j \notin \mathcal{N}(i)$. This ensures that the adjacency matrix $W = [w_{ij}]$ is sparse, consistent with sparse-matrix SGWT implementations.

2.4.2. Edge weights (three strategies)

We compare three edge-weighting strategies on the same 8-neighbor edge set: i) a fixed 8-neighbor lattice (unweighted), for which $w_{ij} = 1$ for $j \in \mathcal{N}(i)$; ii) non-FD similarity weights based only on LD intensities, for which $w_{ij} = \exp\left(-\frac{\|x_i - x_j\|^2}{\sigma^2}\right)$; and iii) the proposed FD-guided similarity weights. FD

guidance is introduced using FD patch intensities on the same patch grid. Let P_i^F denote the FDCT patch aligned with P_i^L. We define the FD descriptor as the vectorized FDCT patch: $\mathbf{f}_i = \mathrm{vec}(P_i^F) \in \mathbb{R}^{p^2}$. The FD-guided edge weight is defined as $w_{ij} = \exp\left(-\frac{\|x_i - x_j\|^2}{\sigma^2}\right) \cdot \exp\left(-\frac{\|f_i - f_j\|^2}{\tau^2}\right)$. In this formulation, σ controls the sensitivity to LD similarity and τ controls the strength of FD guidance.

2.4.3. Intensity scale and parameters

All CT slices were processed in their native intensity scale (Hounsfield units) without min–max normalization. Therefore, the descriptor distances $\| \mathrm{x}_i - \mathrm{x}_j \|_2$ and $\| \mathrm{f}_i - \mathrm{f}_j \|_2$ are computed on a consistent scale across the slices. In our experiments, we fixed $\sigma = 0.5$ and $\tau = 1$ for all the slices. Figure 3 compares the adjacency outcomes produced by the three strategies. Figure 3(a) shows the fixed 8-neighbor grid, Figure 3(b) shows the non-FD similarity graph, and Figure 3(c) shows the proposed FD-guided similarity graph. While the fixed 8-neighbor scheme enforces uniform local connectivity, it does not adapt to structural variation. The non-FD similarity graph is adaptive, but it remains prone to spurious connections. In contrast, the FD-guided graph produces a sparser and more anatomically coherent topology.

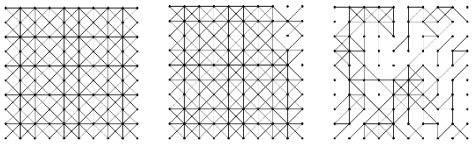

Figure 3. Comparison of adjacency schemes; (a) standard 8-neighbor grid, (b) non-FD similarity graph, and (c) FD-guided similarity graph

2.5. Graph Laplacian and spectral representations

Given the sparse adjacency matrix W, the degree matrix D is diagonal with $D_{ii} = \sum_j w_{ij}$. We use the normalized Laplacian $L = I - D^{-1/2} W D^{-1/2}$. Normalization is commonly used to improve the robustness of the Laplacian spectrum and mitigate sensitivity to noise in graph construction [20]. In the Laplacian spectral domain, low graph frequencies correspond to smoothly varying anatomical structures, whereas high graph frequencies capture rapid variations associated with noise and fine-scale detail. Figure 4 shows representative Laplacian eigenvectors for the non-FD and FD-guided graphs, visualized on the patch grid.

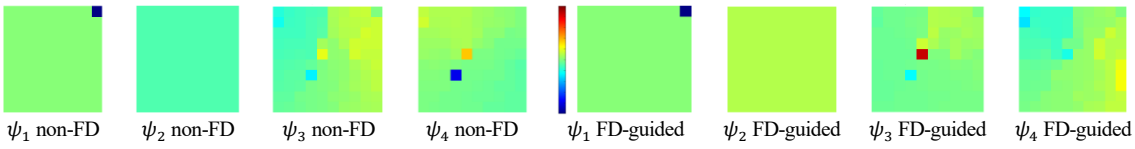

Figure 4. Examples of Laplacian eigenvectors (ψ_1–ψ_4) for non-FD (left) and FD-guided (right) patch graphs reshaped on the patch grid

2.6. Spectral graph wavelet transforms and coefficient shrinkage

SGWT is applied for multiscale spectral filtering on the patch graph constructed for each slice. To avoid explicit eigen decomposition, SGWT operators are evaluated using a Chebyshev polynomial approximation of the spectral kernels, enabling efficient computation via repeated sparse matrix multiplications [21]. In all experiments, we use Chebyshev polynomial order M=30 and the wavelet scales S={0.5, 1, 2}. After computing the SGWT coefficients, noise is suppressed using SURE-based soft thresholding (SUREShrink). Thresholds are selected per scale by minimizing Stein's unbiased risk estimate in the transform domain.

Figure 5 shows the wavelet kernel coverage under unnormalized versus normalized Laplacians. Without normalization, a wide distribution of eigenvalues restricts kernel coverage and reduces the effectiveness of the multiscale representation, as shown in Figure 5(a). Normalization in Figure 5(b) condenses the spectrum, resulting in stable kernel spacing and improved alignment with FD-guided eigenvalues. Figure 6 shows the coefficient maps under non-FD in Figure 6(a) versus FD-guided graphs in Figure 6(b). At finer scales, both non-FD and FD-guided graphs capture local variations, but FD-guided

graphs yield clearer localization. At larger scales, FD-guided graphs better preserve anatomical coherence while suppressing background noise. These results indicate that FD guidance enhances multiscale feature representation, consistent with findings in graph-based image denoising.

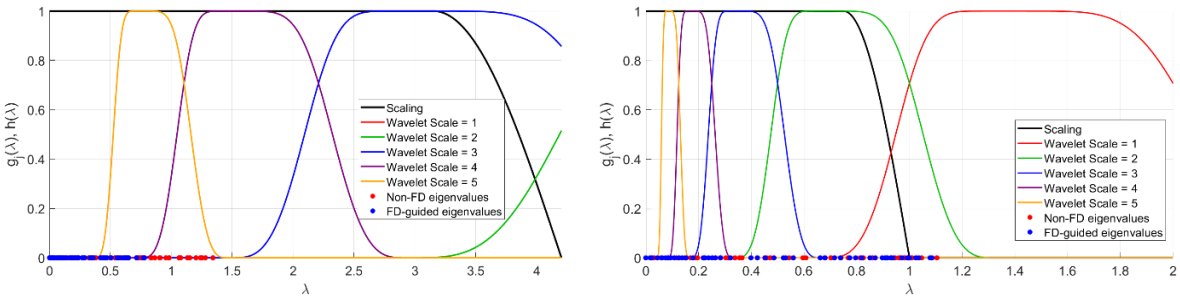

Figure 5. Spectral graph wavelet kernel responses obtained using; (a) unnormalized and (b) normalized Laplacians

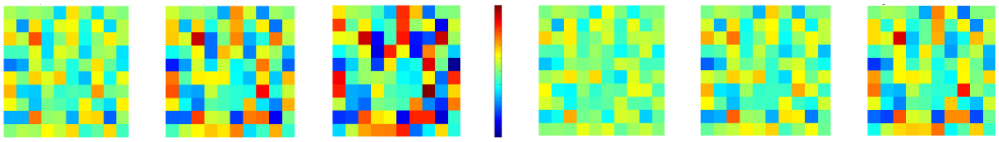

Figure 6. SGWT coefficient maps on a 10×10 patch using; (a) non-FD and (b) FD-guided at scales of 0.5, 1, and 2

2.7. Patch-level reconstruction by overlap-add aggregation

SGWT-domain filtering yields denoised patch signals $\hat{P}_i^L$, which are aggregated to reconstruct the full denoised slice $\hat{I}_L$. We used uniform overlap–add averaging to reduce seam artifacts from patch overlap. Specifically, each pixel is reconstructed as the average of all denoised patches covering that pixel: $\hat{I}_L(u,v) = \frac{1}{C(u,v)} \sum_{i:(u,v)\in\Omega_i} \hat{P}_i^L(u,v)$, where Ω_i is the spatial support of the patch i and $C(u,v)$ counts how many patches cover pixel (u,v). Patch-based denoising commonly reconstructs the full image by aggregating overlapping denoised patches (often via averaging/weighted averaging) to reduce seams and block artifacts [22], [23].

Figures 7–9 illustrate patch-level connectivity differences and the qualitative effect of FD guidance on structural preservation. Figure 7 compares the full-dose reference in Figure 7(a) with the noisy low-dose graph in Figure 7(b).

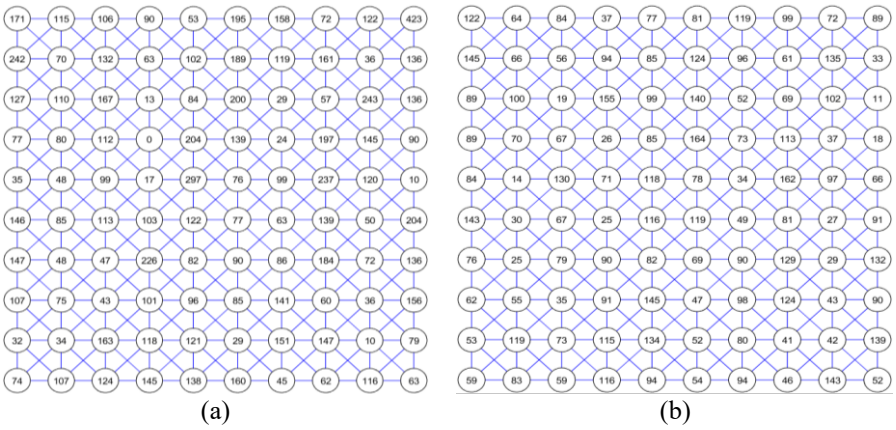

Figure 7. Patch-level comparison; (a) full-dose reference graph and (b) noisy low-dose graph

Figures 8 and 9 show the influence of FD guidance on graph-based denoising. Figures 8(a) and 9(a) indicate that, without FD guidance, changing several vertex values leads to excessive smoothing. In contrast, Figures 8(b) and 9(b) show that, with FD guidance, fewer vertices are altered, resulting in greater stability and better preservation of structural details. These results indicate that FD-guided denoising yields reconstructions that more closely resemble the full-dose reference, while preventing unnecessary alterations.

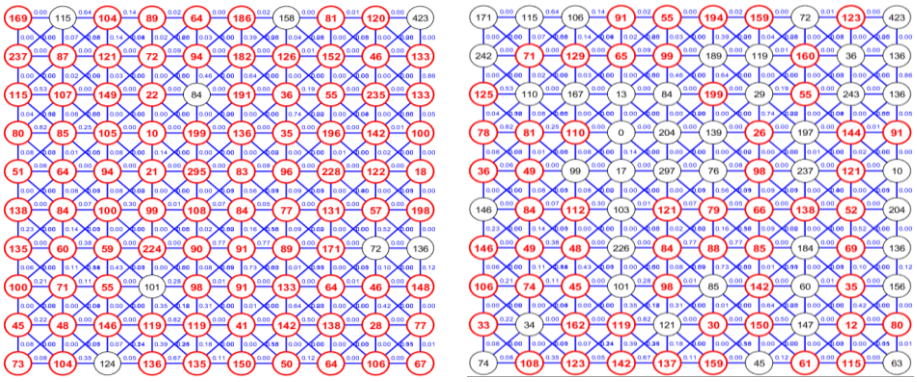

(a) (b)

Figure 8. Patch-level comparison; (a) non-FD over-smooths and (b) FD-guided preserves edges/details

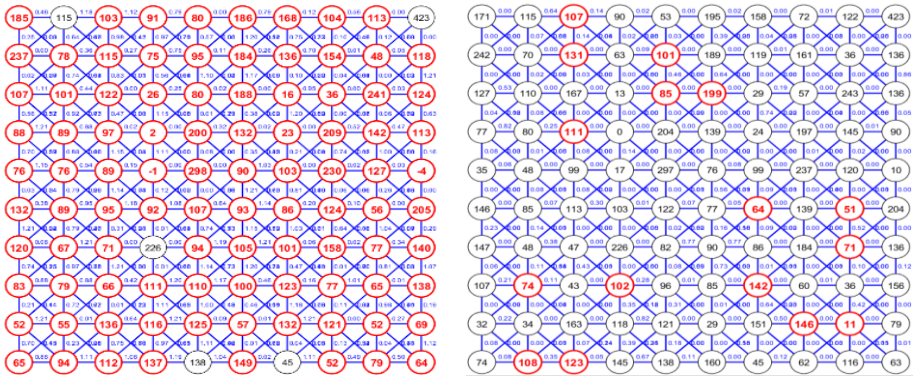

(a) (b)

Figure 9. Patch-level SGWT (SUREShrink); (a) non-FD over-smooths and (b) FD-guided preserves structure

2.8. Evaluation metrics and details of implementation

We evaluate denoising quality against the FDCT reference using PSNR, SSIM, edge preservation index (EPI), and feature similarity index (FSIM).

- PSNR:

$$\text{PSNR} = 10\log_{10}\left(\frac{L^2_{max}}{\text{MSE}}\right) \tag{1}$$

$$MSE = \frac{1}{MN}\sum_{u=1}^{M}\sum_{v=1}^{N}\left(I_F(u,v) - \hat{I}_L(u,v)\right)^2 \tag{2}$$

- SSIM:

$$\text{SSIM}(I_F, \hat{I}_L) = \frac{(2\mu_F\mu_L + C_1)(2\sigma_{FL} + C_2)}{(\mu_F^2 + \mu_L^2 + C_1)(\sigma_F^2 + \sigma_L^2 + C_2)} \tag{3}$$

- EPI:

$$\text{EPI} = \frac{\sum_{i=1}^{MN} \nabla I_F(i) \cdot \nabla \widehat{I_L}(i)}{\sqrt{\sum_{i=1}^{MN} \|\nabla I_F(i)\|_2^2}\sqrt{\sum_{i=1}^{MN} \|\nabla \hat{I}_L(i)\|_2^2}} \tag{4}$$

− FSIM:

$$\mathrm{FSIM}(I_F, \hat{I}_L) = \frac{\sum_{x\in\Omega} PC_m(x)\, S_L(x)\, S_P(x)}{\sum_{x\in\Omega} PC_m(x)} \tag{5}$$

FSIM is widely used as a feature-oriented full-reference metric in image quality evaluation [24]. Edge-focused metrics such as EPI are reported in recent CT denoising evaluations to reflect boundary preservation [25]. All experiments were implemented in MATLAB using sparse matrix operations for graph construction and Chebyshev polynomial approximations for SGWT filtering. Table 1 summarizes the parameter settings for reproducibility.

Table 1. Parameters

Parameter	Meaning	Where used
I_L	LDCT input slice (in Hounsfield units, HU)	Section 2.2–2.8
I_F	Paired FDCT slice used for guidance and as reference	Section 2.2–2.8
p	Patch size (here 10×10)	Vertex definition (section 2.3)
s	Patch stride (here 2)	Patch extraction (section 2.3)
P_i^L	i-th LDCT patch extracted from the I_L	Section 2.3–2.4
P_i^F	FDCT patch aligned with P_i^L, extracted from I_F	Section 2.4
$\mathbf{x}_i$	LD vertex descriptor: $\mathbf{x}_i = \mathrm{vec}(P_i^L) \in \mathbb{R}^{p^2}$	Vertex labels (section 2.3–2.4)
$\mathbf{f}_i$	FD guidance descriptor (new explicit definition): $\mathbf{f}_i = \mathrm{vec}(P_i^F) \in \mathbb{R}^{p^2}$	FD-guided weights (section 2.4)
V	Vertex set (one vertex per patch)	Graph definition (section 2.3)
$\mathcal{N}(i)$	8-neighbor set on the patch grid (sparse topology)	Edge set (section 2.4)
E	Edge set restricted to $j \in \mathcal{N}(i)$ (no dense all-pair edges)	Section 2.4
$W = [w_{ij}]$	Sparse adjacency matrix (weights only for $j \in \mathcal{N}(i)$)	Section 2.4–2.5
σ	LD similarity scale (here 0.5); controls the sensitivity of $\| \mathbf{x}_i - \mathbf{x}_j \|_2$	FD/non-FD weights (section 2.4)
τ	FD guidance scale (here 1); controls the sensitivity of $\| \mathbf{f}_i - \mathbf{f}_j \|_2$	FD-guided weights (section 2.4)
w_{ij} (non-FD)	$w_{ij} = \exp(-\| \mathbf{x}_i - \mathbf{x}_j \|_2^2/\sigma^2)$, for $j \in \mathcal{N}(i)$	Baseline adjacency (section 2.4)
w_{ij} (FD-guided)	$w_{ij} = \exp(-\| \mathbf{x}_i - \mathbf{x}_j \|_2^2/\sigma^2) \cdot \exp(-\| \mathbf{f}_i - \mathbf{f}_j \|_2^2/\tau^2)$, for $j \in \mathcal{N}(i)$	Proposed adjacency (section 2.4)
D	Degree matrix, $D_{ii} = \sum_j w_{ij}$	Laplacian (section 2.5)
L	Normalized Laplacian, $L = I - D^{-1/2} W D^{-1/2}$	Section 2.5–2.6
SGWT scales S	Multiscale set $S = \{0.5, 1.0, 2.0\}$	SGWT (section 2.6)
M	Chebyshev polynomial order (here 30) for fast SGWT approximation	SGWT computation (section 2.6)
$T(\cdot)$	Shrinkage operator: SURE-based soft-threshold (SUREShrink), per scale	Denoising (section 2.6)
ω	Overlap–add aggregation weights (uniform $\omega = 1$, i.e., pixel-wise averaging)	Reconstruction (section 2.7)
Metrics	PSNR, SSIM, EPI, and FSIM (computed vs. FDCT reference)	Section 2.8
Implementation	MATLAB (sparse matrices for W, L; Chebyshev SGWT), CPU execution	Section 2.8, Table 1

3. RESULTS AND DISCUSSION

This section evaluates the proposed FD-guided patch-graph denoising framework described in section 2. The method aims to suppress LDCT noise while preserving anatomically meaningful edges and fine structures by transferring structural information from FDCT into graph construction. We report: i) qualitative comparisons on representative regions of interest and ii) quantitative performance of PSNR, SSIM, EPI, and FSIM over all 318 LDCT slices. Comparisons against non-FD graph baselines were used to isolate the effect of FD-guided vertex and edge labelling.

3.1. Qualitative evaluation

Figure 10 shows a representative visual comparison using a localized region of interest (ROI) to emphasize fine structural details that may be obscured at the full-slice scale. Figure 10(a) shows the FD image with the ROI marked. The FDCT reference ROI in Figure 10(b) exhibits elongated vessel-like structures with clear boundaries, whereas the LDCT ROI in Figure 10(c) contains strong noise that reduces edge visibility. The non-FD graph denoising baseline in Figure 10(d) suppresses noise but introduces noticeable smoothing and residual artifacts that partially attenuate thin structures.

In contrast, the proposed FD-guided graph denoising results shown in Figures 10(e) and (f) better preserve directional boundaries and local continuity, indicating that FD-informed edge labelling yields anatomically coherent patch connectivity. The FD-guided SGWT result further improves boundary sharpness and local contrast, producing the closest visual match to the FDCT reference among the methods compared. Overall, FD guidance stabilizes graph construction and improves the structural selectivity of SGWT-based filtering, especially in regions with fine textures and anisotropic features such as vessels and tissue interfaces.

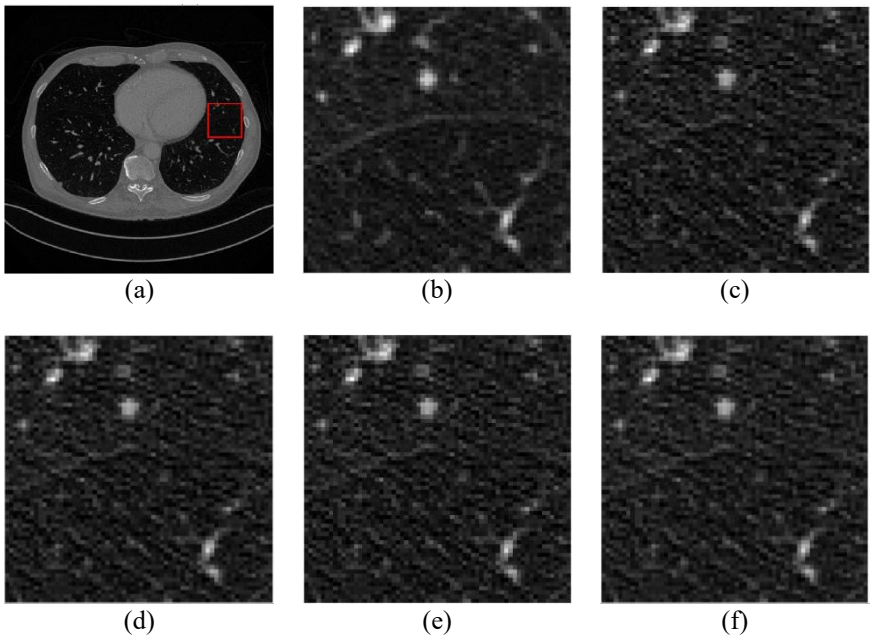

Figure 10. Representative qualitative comparison on a slice and localized ROI; (a) FDCT slice with highlighted ROI, (b) FDCT ROI (reference), (c) LDCT ROI (noisy input), (d) non-FD graph denoising (LD-driven weights), (e) FD-guided graph denoising, and (f) FD-guided SGWT denoising

3.2. Quantitative evaluation

Quantitative evaluation is performed over all 318 slices using PSNR, SSIM, EPI, and FSIM with the paired FDCT images as references. Figures 11–14 report metric values per slice for each method. As expected, the LDCT baseline produces the lowest scores due to substantial noise and artifact contamination. The non-FD SGWT baseline provides limited improvement, which is consistent with the fact that its Laplacian is derived from noisy LDCT intensities and can yield unstable spectral representations. Figure 11 shows PSNR values across all 318 LDCT slices, where higher PSNR indicates greater fidelity to the FDCT reference. Figure 12 presents SSIM values across the same slices, where higher SSIM reflects improved structural similarity to the FDCT reference. Figure 13 reports FSIM values, where higher FSIM indicates better structural preservation. Figure 14 displays EPI values, where higher EPI indicates stronger edge alignment between the denoised output and the FDCT reference.

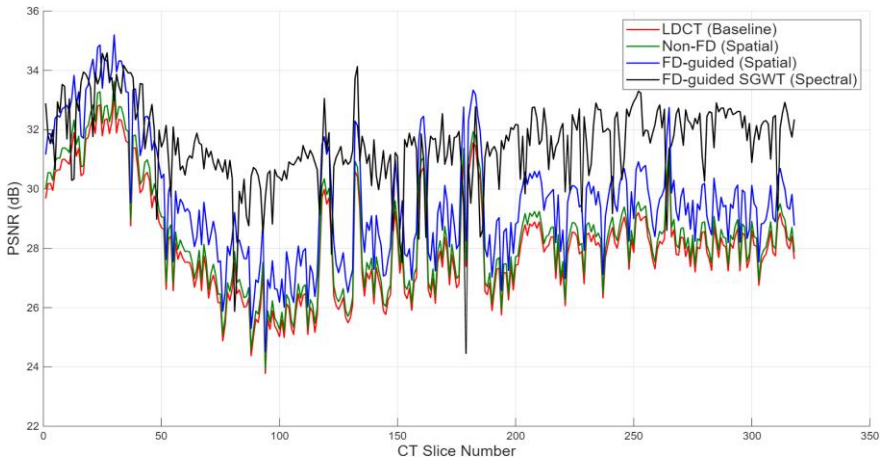

Figure 11. PSNR across all 318 LDCT slices

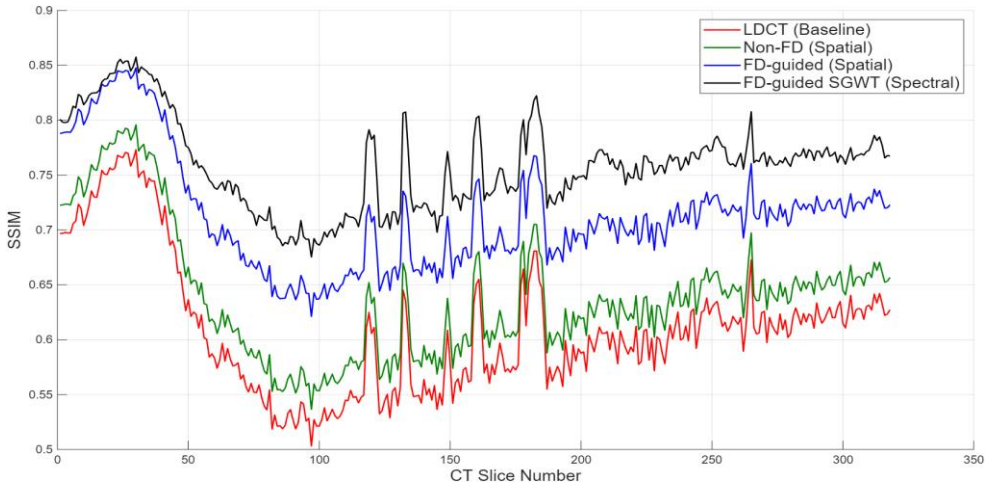

Figure 12. SSIM across all 318 LDCT slices

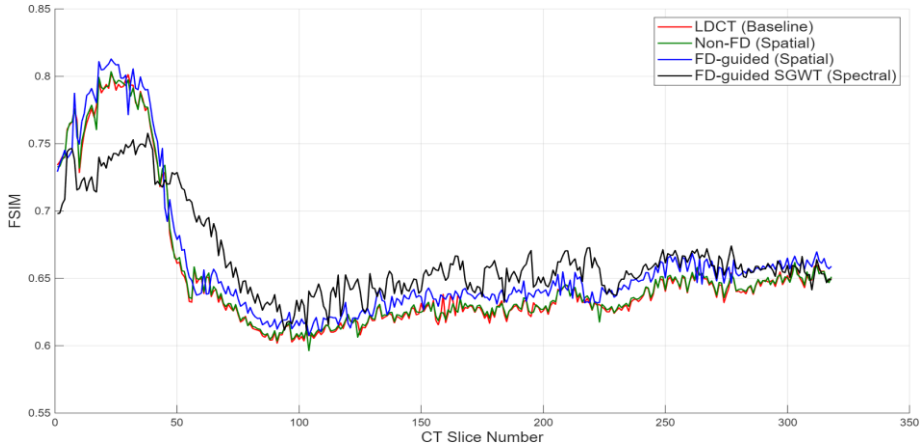

Figure 13. FSIM across all 318 LDCT slices

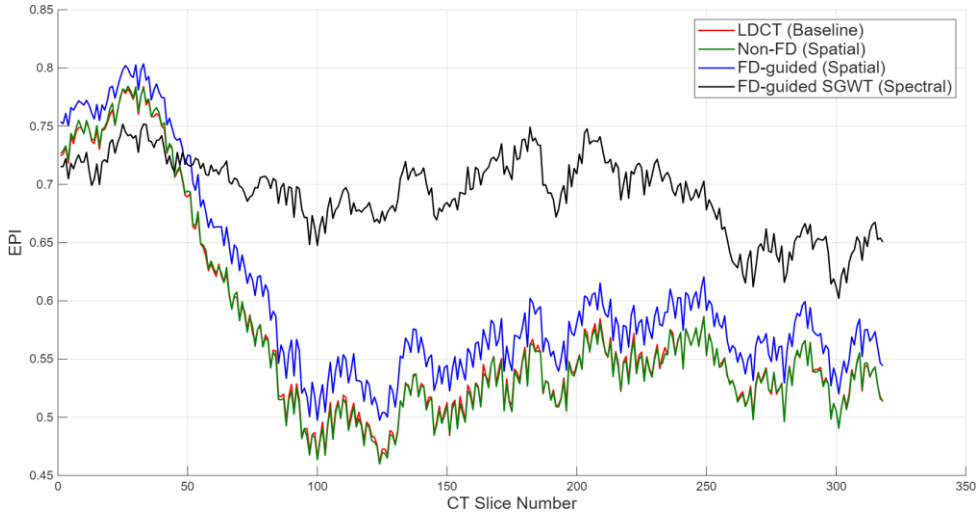

Figure 14. EPI across all 318 LDCT slices

FD-guided methods achieve consistently higher scores across all metrics, demonstrating improved noise suppression and structural information preservation. In particular, the FD-guided SGWT achieved the strongest overall performance in SSIM, EPI, and FSIM, reflecting superior retention of edges and perceptually relevant structures while reducing noise. Although FDCT information is used during graph construction, the denoised output remains governed by LDCT intensity statistics because no explicit FDCT intensity constraint is enforced; therefore, minor intensity bias relative to FDCT may persist even when structural fidelity improves. This behavior motivates future work on integrating explicit intensity calibration or bias-correction strategies alongside FD-guided topology stabilization.

3.3. Comparison with the existing computed tomography denoising methods

Recent research on LDCT denoising is dominated by learning-based methods, including CNNs, CNN–Transformer hybrids, and diffusion-based priors. CNN–Transformer hybrid designs leverage convolution for local feature extraction and attention for longer-range context modeling, and they have reported strong PSNR/SSIM performance on public LDCT benchmarks [16], [26]. Self-supervised approaches aim to reduce the reliance on paired targets; for example, structure-guided pipelines construct guidance images or structural priors to mitigate over-smoothing while training without clean references [27]. Diffusion priors have been explored for zero-shot or weakly supervised denoising, leveraging generative priors but typically requiring iterative inference and careful tuning to avoid content drift [28]. Recent benchmarking studies further highlight that the reported improvements across deep learning LDCT denoisers can be marginal under standardized evaluation protocols, motivating transparent and reproducible comparisons [29]. In parallel, surveys of unsupervised and self-supervised LDCT denoising emphasize that training strategy and noise assumptions can strongly affect robustness and artifact behavior [30], and projection-domain self-supervised approaches have also been demonstrated for LDCT settings without clean references [31].

In contrast to these learning-based families, the proposed approach is training-free and operates entirely within a GSP framework. The key difference from conventional graph denoisers is explicit FD-guided vertex and edge labelling: FDCT guidance stabilizes the adjacency structure and Laplacian spectrum, improving the reliability of SGWT-domain filtering. This complements learning-based approaches by offering a parameter-transparent pipeline whose behavior can be analyzed using graph topology and Laplacian spectra. This yields improved PSNR/SSIM and stronger edge/feature preservation (EPI/FSIM) relative to non-guided graph baselines, while maintaining interpretability and avoiding the data requirements of supervised deep networks. These characteristics position FD-guided graph labelling as a complementary alternative in scenarios where training data are limited or when robustness and transparency are prioritized.

4. CONCLUSION

This paper presented an FD-guided graph-based LDCT denoising framework that explicitly incorporates vertex and edge labelling to stabilize graph construction for spectral filtering. The proposed FD-guided affinity reduces noise-induced distortions in the Laplacian spectrum and enables reliable multiscale denoising via SGWT. This is achieved by transferring structural guidance from paired FDCT images to the LDCT patch graph. Experiments on paired LDCT/FDCT slices demonstrate consistent improvements over non-guided graph baselines, yielding higher PSNR/SSIM and stronger edge/feature preservation (EPI/FSIM), with improved directional anatomical structure retention. The current evaluation is limited to a single-patient dataset, and the method incurs nontrivial computational cost due to patch-graph construction and multiscale spectral transforms. Future work will validate robustness on multi-patient cohorts (cross-patient splits and scanner/dose variability), accelerate computation via sparse neighborhood design and approximate spectral operators, and explore hybrid integration of FD-guided graph representations with learning-based denoisers to improve generalization.

ACKNOWLEDGMENT

This research is part of Iwan Setiawan's doctoral research, funded by the Degree by Research Scholarship, National Research and Innovation Agency, Indonesia (DBR-BRIN).

FUNDING INFORMATION

This research was funded by the Degree by Research Scholarship, National Research and Innovation Agency (DBR-BRIN), Indonesia.

AUTHOR CONTRIBUTIONS STATEMENT

This journal uses the Contributor Roles Taxonomy (CRediT) to recognize individual author contributions, reduce authorship disputes, and facilitate collaboration.

Name of Author	C	M	So	Va	Fo	I	R	D	O	E	Vi	Su	P	Fu
Iwan Setiawan	✓	✓	✓	✓	✓	✓	✓	✓	✓	✓	✓			
Didi Rosiyadi		✓								✓		✓		
Rina Ratianingsih					✓				✓					
Maulidyani Abu						✓			✓					
Edy Tri Baskoro	✓									✓		✓		

C : **C**onceptualization
M : **M**ethodology
So : **So**ftware
Va : **Va**lidation
Fo : **Fo**rmal analysis
I : **I**nvestigation
R : **R**esources
D : **D**ata Curation
O : Writing - **O**riginal Draft
E : Writing - Review & **E**diting
Vi : **Vi**sualization
Su : **Su**pervision
P : **P**roject administration
Fu : **Fu**nding acquisition

CONFLICT OF INTEREST STATEMENT

The authors have no conflicts of interest.

DATA AVAILABILITY

The data supporting the findings of this study are publicly available at https://www.kaggle.com/datasets/andrewmvd/ct-low-dose-reconstruction [17].

REFERENCES

[1] P. Mohammadinejad *et al.*, "Ct noise-reduction methods for lower-dose scanning: Strengths and weaknesses of iterative reconstruction algorithms and new techniques," *Radiographics*, vol. 41, no. 5, pp. 1493–1508, Sep. 2021, doi: 10.1148/rg.2021200196.

[2] D. C. Lepcha *et al.*, "Low-dose computed tomography image denoising using pixel level non-local self-similarity prior with non-local means for healthcare informatics," *Sci. Rep.*, vol. 15, no. 1, p. 25095, Jul. 2025, doi: 10.1038/s41598-025-10139-2.

[3] F. D. Feola, L. Tronchin, V. Guarrasi, and P. Soda, "Multi-scale texture loss for CT denoising with GANs," *AI Open*, vol. 6, pp. 142–154, 2025, doi: 10.1016/j.aiopen.2025.09.001.

[4] R. T. Sadia, J. Chen, and J. Zhang, "CT image denoising methods for image quality improvement and radiation dose reduction," *J. Appl. Clin. Med. Phys.*, vol. 25, no. 2, Feb. 2024, doi: 10.1002/acm2.14270.

[5] S. Bhadra, V. A. Kelkar, F. J. Brooks, and M. A. Anastasio, "On Hallucinations in Tomographic Image Reconstruction," *IEEE Trans. Med. Imaging*, vol. 40, no. 11, pp. 3249–3260, 2021, doi: 10.1109/TMI.2021.3077857.

[6] S. S. Chen, H. H. Liu, and C. C. Yang, "Evaluating the impact of deep learning-based image denoising on low-dose CT for lung cancer screening," *J. Appl. Clin. Med. Phys.*, vol. 27, no. 2, Feb. 2026, doi: 10.1002/acm2.70480.

[7] W. Kim, S. Y. Jeon, G. Byun, H. Yoo, and J. H. Choi, "A systematic review of deep learning-based denoising for low-dose computed tomography from a perceptual quality perspective," *Biomed. Eng. Lett.*, vol. 14, no. 6, pp. 1153–1173, Nov. 2024, doi: 10.1007/s13534-024-00419-7.

[8] X. Liu *et al.*, "Diffusion probabilistic priors for zero-shot low-dose CT image denoising," *Med. Phys.*, vol. 52, no. 1, pp. 329–345, Jan. 2025, doi: 10.1002/mp.17431.

[9] G. Leus, A. G. Marques, J. M. F. Moura, A. Ortega, and D. I. Shuman, "Graph Signal Processing: History, development, impact, and outlook," *IEEE Signal Process. Mag.*, vol. 40, no. 4, pp. 49–60, Jun. 2023, doi: 10.1109/MSP.2023.3262906.

[10] M. Cheung, J. Shi, O. Wright, L. Y. Jiang, X. Liu, and J. M. F. Moura, "Graph Signal Processing and Deep Learning: Convolution, Pooling, and Topology," *IEEE Signal Process. Mag.*, vol. 37, no. 6, pp. 139–149, Nov. 2020, doi: 10.1109/MSP.2020.3014594.

[11] X. Dong, D. Thanou, L. Toni, M. Bronstein, and P. Frossard, "Graph Signal Processing for Machine Learning: A Review and New Perspectives," *IEEE Signal Process. Mag.*, vol. 37, no. 6, pp. 117–127, Nov. 2020, doi: 10.1109/MSP.2020.3014591.

[12] X. Ding and H. T. Wu, "Impact of Signal-to-Noise Ratio and Bandwidth on Graph Laplacian Spectrum From High-Dimensional Noisy Point Cloud," *IEEE Trans. Inf. Theory*, vol. 69, no. 3, pp. 1899–1931, Mar. 2023, doi: 10.1109/TIT.2022.3216561.

[13] L. Jiao *et al.*, "Graph Representation Learning Meets Computer Vision: A Survey," *IEEE Trans. Artif. Intell.*, vol. 4, no. 1, pp. 2–22, Feb. 2023, doi: 10.1109/TAI.2022.3194869.

[14] B. de Loynes, F. Navarro, and B. Olivier, "Data-driven thresholding in denoising with Spectral Graph Wavelet Transform," *J. Comput. Appl. Math.*, vol. 389, p. 113319, Jun. 2021, doi: 10.1016/j.cam.2020.113319.

[15] M. Zubair, H. B. Md Rais, F. Ullah, Q. Al-Tashi, M. Faheem, and A. A. Khan, "Enabling Predication of the Deep Learning Algorithms for Low-Dose CT Scan Image Denoising Models: A Systematic Literature Review," *IEEE Access*, vol. 12, pp. 79025–79050, 2024, doi: 10.1109/ACCESS.2024.3407774.

[16] S. Y. Zhang *et al.*, "Hformer: highly efficient vision transformer for low-dose CT denoising," *Nucl. Sci. Tech.*, vol. 34, no. 4, p. 61, Apr. 2023, doi: 10.1007/s41365-023-01208-0.

[17] "CT Low Dose Reconstruction, Kaggle dataset". [Online]. Available: https://www.kaggle.com/datasets/andrewmvd/ct-low-dose-reconstruction. (Accessed: Feb. 9, 2026).

[18] T. R. Moen *et al.*, "Low-dose CT image and projection dataset," *Med. Phys.*, vol. 48, no. 2, pp. 902–911, Feb. 2021, doi: 10.1002/mp.14594.
[19] J. Leuschner, M. Schmidt, D. O. Baguer, and P. Maass, "LoDoPaB-CT, a benchmark dataset for low-dose computed tomography reconstruction," *Sci. Data*, vol. 8, no. 1, p. 109, Apr. 2021, doi: 10.1038/s41597-021-00893-z.
[20] X. Cheng and B. Landa, "Bi-stochastically normalized graph Laplacian: convergence to manifold Laplacian and robustness to outlier noise," *Inf. Inference*, vol. 13, no. 4, Sep. 2024, doi: 10.1093/imaiai/iaae026.
[21] E. Isufi, F. Gama, D. I. Shuman, and S. Segarra, "Graph Filters for Signal Processing and Machine Learning on Graphs," *IEEE Trans. Signal Process.*, vol. 72, pp. 4745–4781, 2024, doi: 10.1109/TSP.2024.3349788.
[22] H. Shi, Y. Traonmilin, and J. F. Aujol, "Compressive Learning for Patch-Based Image Denoising," *SIAM J. Imaging Sci.*, vol. 15, no. 3, pp. 1184–1212, Sep. 2022, doi: 10.1137/21M1459812.
[23] S. Tabassum and S. K. C. Gowre, "Optimal image Denoising using patch-based convolutional neural network architecture," *Multimed. Tools Appl.*, vol. 82, no. 19, pp. 29805–29821, Aug. 2023, doi: 10.1007/s11042-023-15014-8.
[24] T. Islam and S. R. Islam, "A New Image Quality Index and it"s Application on MRI Image," *Int. J. Image, Graph. Signal Process.*, vol. 13, no. 4, pp. 14–32, Aug. 2021, doi: 10.5815/ijigsp.2021.04.02.
[25] F. Mattiussi *et al.*, "ErisNet: A Deep Learning Model for Noise Reduction in CT Images," *Bioengineering*, vol. 12, no. 9, p. 997, Sep. 2025, doi: 10.3390/bioengineering12090997.
[26] J. Yuan, F. Zhou, Z. Guo, X. Li, and H. Yu, "HCformer: Hybrid CNN-Transformer for LDCT Image Denoising," *J. Digit. Imaging*, vol. 36, no. 5, pp. 2290–2305, Jun. 2023, doi: 10.1007/s10278-023-00842-9.
[27] Q. Wu *et al.*, "Unsharp Structure Guided Filtering for Self-Supervised Low-Dose CT Imaging," *IEEE Trans. Med. Imaging*, vol. 42, no. 11, pp. 3283–3294, Nov. 2023, doi: 10.1109/TMI.2023.3280217.
[28] F. N. Mazandarani, P. Babyn, and J. Alirezaie, "SADiff: A Sinogram-Aware Diffusion Model for Low-Dose CT Image Denoising," *J. Imaging Informatics Med.*, vol. 38, no. 6, pp. 4255–4275, Mar. 2025, doi: 10.1007/s10278-025-01469-8.
[29] E. Eulig, B. Ommer, and M. Kachelrieß, "Benchmarking deep learning-based low-dose CT image denoising algorithms," *Med. Phys.*, vol. 51, no. 12, pp. 8776–8788, Dec. 2024, doi: 10.1002/mp.17379.
[30] F. Zhao *et al.*, "Unsupervised and Self-supervised Learning in Low-Dose Computed Tomography Denoising: Insights from Training Strategies," *J. Imaging Informatics Med.*, vol. 38, no. 2, pp. 902–930, Sep. 2025, doi: 10.1007/s10278-024-01213-8.
[31] K. Choi, S. H. Kim, and S. Kim, "Self-supervised denoising of projection data for low-dose cone-beam CT," *Med. Phys.*, vol. 50, no. 10, pp. 6319–6333, Oct. 2023, doi: 10.1002/mp.16421.

BIOGRAPHIES OF AUTHORS

Iwan Setiawan received his Master of Engineering degree from Institut Teknologi Bandung, Indonesia. He is a student of the Doctoral Program of Mathematics, Faculty of Mathematics and Natural Sciences, Institut Teknologi Bandung, Indonesia. He is a researcher at the Research Center for Artificial Intelligence and Cyber Security, National Research and Innovation Agency, Bandung, Indonesia. He is also a member of the Center for Research Collaboration on Graph Theory and Combinatorics in Indonesia. His research interests include graph theory, signal and image processing. He can be contacted at email: iwan022@brin.go.id.

Didi Rosiyadi holds a Ph.D. degree in Information Security from the National Taiwan University of Science and Technology. He is a research professor at the Research Center for Artificial Intelligence and Cyber Security, National Research and Innovation Agency, Indonesia. He is also a member of the Center for Research Collaboration on Graph Theory and Combinatorics in Indonesia. His research interests include data and information security. He can be contacted at email: didi016@brin.go.id.

Rina Ratianingsih received her M.Sc. degree in applied mathematics from the Institut Teknologi Bandung. She is currently a lecturer in the department of Physics and Mathematics, Faculty of Mathematics and Natural Science, University of Tadulako, Indonesia. Her research interest is applied mathematics. She can be contacted at email: ratianingsihrina8@gmail.com.

Maulidyani Abu received a bachelor's degree in the Mathematics Study Program with a focus on optimal control research from Tadulako University and a master's degree in the Mathematics Study Program from the Sepuluh Nopember Institute of Technology, specializing in magnetohydrodynamics. She is a mathematics lecturer at Tadulako University. Her research interests are in applied mathematics. She can be contacted at email: maulidyanisho7992@gmail.com.

Edy Tri Baskoro holds a Ph.D. in Mathematics from the University of Newcastle, Australia, in 1996. His current position is a Professor in Mathematics at Institut Teknologi Bandung, Indonesia. Since July 2022, he has been the Chair of the Center of Research and Collaboration on Graph Theory and Combinatorics in Indonesia. He served as a Conjoint Professor at The School of Electrical Engineering and Computer Science, University of Newcastle, Australia (2006-2015), and The Abdus Salam School of Mathematical Sciences, GC University, Lahore Pakistan (2006-2015). His research interests include Ramsey theory, extremal problems in graphs, distance in graphs, graph labelling, graph coloring, and graph algorithms. He can be contacted at email: ebaskoro@itb.ac.id.